JCIM JOURNAL OF CHEMICAL INFORMATION AND MODELING

pubs.acs.org/jcim Article

Effect of Cysteine Oxidation in SARS-CoV-2 Receptor-Binding Domain on Its Interaction with Two Cell Receptors: Insights from Atomistic Simulations

Maryam Ghasemitarei,* Angela Privat-Maldonado, Maksudbek Yusupov, Shadi Rahnama, Annemie Bogaerts, and Mohammad Reza Ejtehadi*

Cite This: J. Chem. Inf. Model. 2022, 62, 129−141 Read Online

ACCESS | Metrics & More | Article Recommendations | Supporting Information

ABSTRACT: Binding of the SARS-CoV-2 S-glycoprotein to cell receptors is vital for the entry of the virus into cells and subsequent infection. ACE2 is the main cell receptor for SARS-CoV-2, which can attach to the C-terminal receptor-binding domain (RBD) of the SARS-CoV-2 S-glycoprotein. The GRP78 receptor plays an anchoring role, which attaches to the RBD and increases the chance of other RBDs binding to ACE2. Although high levels of reactive oxygen and nitrogen species (RONS) are produced during viral infections, it is not clear how they affect the RBD structure and its binding to ACE2 and GRP78. In this research, we apply molecular dynamics simulations to study the effect of oxidation of the highly reactive cysteine (Cys) amino acids of the RBD on its binding to ACE2 and GRP78. The interaction energy of both ACE2 and GRP78 with the whole RBD, as well as with the RBD main regions, is compared in both the native and oxidized RBDs. Our results show that the interaction energy between the oxidized RBD and ACE2 is strengthened by 155 kJ/mol, increasing the binding of the RBD to ACE2 after oxidation. In addition, the interaction energy between the RBD and GRP78 is slightly increased by 8 kJ/mol after oxidation, but this difference is not significant. Overall, these findings highlight the role of RONS in the binding of the SARS-CoV-2 S-glycoprotein to host cell receptors and suggest an alternative mechanism by which RONS could modulate the entrance of viral particles into the cells.

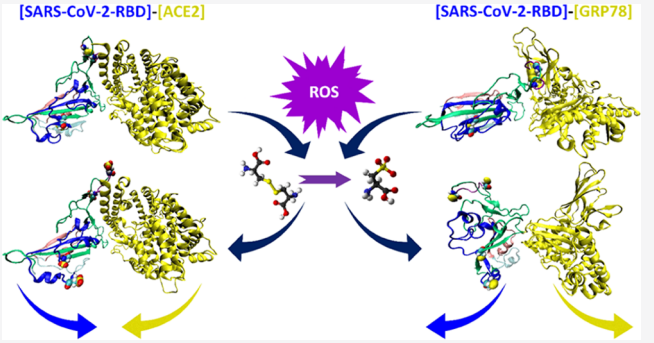

1. INTRODUCTION

At the end of 2019, a new virus showing general symptoms such as fever, dyspnea, dry cough, and tiredness in most people was discovered in Wuhan city, China. This virus has affected over 187 million people since then and killed more than 4 million in various countries (data obtained from ref 1, corresponding to July 11, 2021). The virus is a member of the coronavirus family, which causes coronavirus disease 2019 (COVID-19). The International Committee on Taxonomy of Viruses (ICTV) officially designated the virus as severe acute respiratory syndrome coronavirus 2 (SARS-CoV-2). SARS-CoV-2 is the seventh coronavirus that can infect humans,[2] with SARS-CoV and MERS-CoV being the ones with the highest infection and mortality rates (10 and 36%, respectively[3]). While the wild type of SARS-CoV-2 has only a 2% mortality rate, the fast human-to-human transmission of this virus makes it a Public Health Emergency of International Concern (PHEIC).[4]

Structural proteins play an important role in pathogenesis, as well as in the assembly and structure of virions. Among all structural proteins, a densely glycosylated S on the virion's outer surface is responsible for virus attachment and entry to the host cells.[5] The S-glycoprotein is a trimeric class I fusion protein that exists in a metastable prefusion conformation that undergoes a substantial structural rearrangement to fuse the viral and host cell membrane together. The S-glycoprotein contains two functional subunits S_1 and S_2, which are responsible for binding to the host cell receptor and for fusion of the viral and cellular membranes, respectively. Entry to the host cell is triggered when the receptor-binding domain (RBD) of the S_1 subunit binds to a host cell receptor. Receptor-binding destabilizes the prefusion trimer, resulting in shedding of the S_1 subunit and transition of the S_2 subunit to a stable postfusion conformation.[6] The S_1 subunit of different coronaviruses uses two distinct domains to recognize a variety of attachments and entry receptors, depending on the viral

Received: July 15, 2021
Published: December 30, 2021

https://doi.org/10.1021/acs.jcim.1c00853
J. Chem. Inf. Model. 2022, 62, 129−141

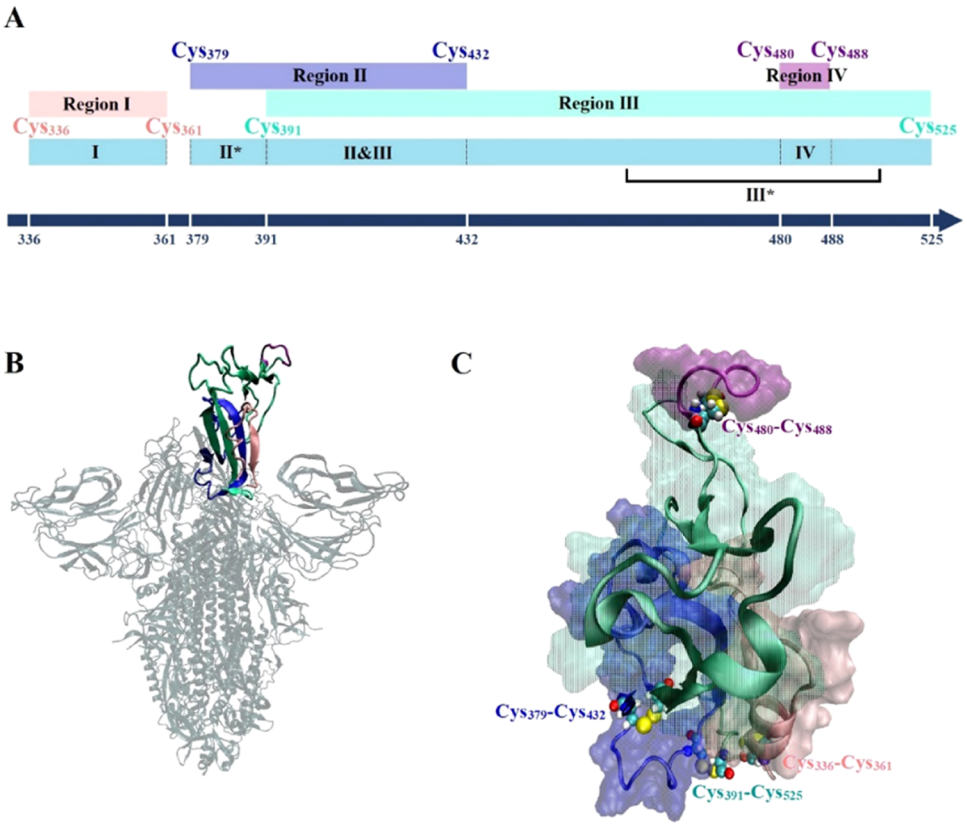

Figure 1. (A) Regions I (Cys_{336}–Cys_{361}), II (Cys_{379}–Cys_{432}), III (Cys_{391}–Cys_{525}), and IV (Cys_{480}–Cys_{488}), determined by Ibrahim et al.,[12] are shown schematically by pink, dark-blue, light-green, and purple boxes, respectively. The nonoverlapping regions (I, II*, II&III, III*, and IV) of RBD with the new definition are shown schematically in the bottom row. The sequence numbers for the regions are indicated in the blue axis (the scale is not uniform). (B) New-cartoon representation of RBD exposed to its receptor (not shown here) with multiple colors in the S-glycoprotein (dark cyan). (C) The close-up view of RBDs with multiple colors shown by new-cartoon and surface representations as well as all Cys residues of RBD are shown by a ball and stick representation.

species. Generally, S_1 consists of two domains, the N-terminal domain (NTD) and the C-terminal domain (CTD), both of which can function as a receptor-binding entity (e.g., SARS-CoV and MERS-CoV utilize the S_1 CTD as an RBD).[7] The coronavirus S-glycoprotein is surface-exposed and mediates entry into host cells, which makes it the main target of neutralizing antibodies and an attractive option for the development of therapeutic agents and vaccines.

The S-glycoprotein of SARS-CoV, and several other SARS-related coronaviruses, interacts directly with the angiotensin-converting enzyme 2 (ACE2) on target cells.[8] ACE2 is an enzyme attached to the membranes of cells in lungs, arteries, heart, kidney, and intestines.[9] SARS-CoV-2 S_1 CTD (referred to as RBD henceforth) has been identified as a key region of SARS-CoV-2 that interacts with the ACE2 receptor.[8] Walls et al.[10] reported that ACE2 could facilitate SARS-CoV-2 S-mediated entry into cells, establishing it as a functional receptor for this virus. Another protein, glucose regulating protein 78 (GRP78, or binding immunoglobulin protein), which could facilitate MERS-CoV and bat coronavirus HKU9 entry into permissive cells by enhancing virus attachment,[11] was also identified as a receptor for SARS-CoV-2 S-glycoprotein.[12] A significantly higher level of GRP78 in patients with SARS-CoV-2 compared to healthy patients highlights the importance of the GRP78 receptor.[13] GRP78 is the master chaperone protein of the unfolded protein response.[5] Under normal conditions, GRP78 is found in the lumen of the endoplasmic reticulum (ER), which inactivates three enzymes responsible for cell death or differentiation. Overexpression of GRP78 is initiated upon cell stress, which increases GRP78 translocation to the cell membrane. Cell surface GRP78 is susceptible to virus recognition by its substrate-binding domain (SBD), and it can mediate the virus entry in the cell.[12] Recently, Ibrahim et al. introduced GRP78 as another receptor for SARS-CoV-2 S-glycoprotein using molecular docking simulations.[12] The authors suggested that this receptor facilitates the attachment of the virus to the surface of the host cell, exploring potential interactions between GRP78 and S-glycoprotein. Following them, Allam et al. identified some small peptides and molecules that can disturb the interaction of target cells with SARS-CoV-2 by inhibiting the recognition of GRP78 by the SARS-CoV-2 S-glycoprotein.[14] Furthermore, experimental studies have shown GRP78 as an important secondary factor for the entry and infection of SARS-CoV-2,[15] which also increases host cell recognition in the new U.K. variant of SARS-CoV-2.[16] Thus, GRP78 could be a potential therapeutic target for reducing SARS-CoV-2 infection.

ACE2 and GRP78 have strong affinity to RBD.[7,12] Studying the interaction of RBD with these receptors, and in particular, identifying the important residues that are the most effective in RBD-cell receptor affinity, is essential. Previous atomic-level investigations on RBD and its binding with ACE2 or GRP78 revealed useful information about the interactions between amino acids of these proteins.[7,12] However, viral infections are linked to the overproduction of reactive oxygen and nitrogen

https://doi.org/10.1021/acs.jcim.1c00853
J. Chem. Inf. Model. 2022, 62, 129−141

species (RONS) and deprived antioxidant systems that result from the cytokine response, inflammation, and cell death induced to eliminate the pathogens.[17,18] It has been proposed that the SARS-CoV-2 virus is able to promote a chronic state of inflammation in host cells to maintain a state of oxidative stress.[19] Interestingly, the ACE2 receptor plays a key role in lowering oxidative stress: membrane-bound ACE2 degrades Angiotensin II, which induces RONS production by membrane-bound NADPH oxidase. The resulting product, Angiotensin 1−7, inhibits NADPH oxidase. However, when ACE2 is bound to the SARS-CoV-2 S-glycoprotein, it cannot degrade Angiotensin II, thus increasing RONS levels at the cell surface and creating a cycle of oxidative stress in the cells.[20] It is known that RONS can cause oxidation and nitration of amino acids in proteins, which can disturb their normal functioning.[21−26]

Experiments performed using an external RONS source (cold atmospheric plasma) revealed that the highly reactive amino acids Met and cysteine (Cys) are primarily oxidized in aqueous solutions (see the Supporting Information (SI)). Due to the absence of Met residues in the RBD structure, it is possible that Cys residues are initially oxidized. A previous study showed that the oxidation pathways of Cys are related to the structure of the oxidant and the reaction conditions.[27] Another study on the products of Cys oxidation by an external RONS source reported that Cys oxidation has two main products: cystine (disulfide bond formation between two cysteine residues) and cysteic acid.[28−31] Since all Cys residues of the RBD in the native structure make disulfide bonds with each other, oxidation of the residues by excessive RONS will produce cysteic acids. This could subsequently influence the interaction of RBD with ACE2 and GRP78. Recently, it has been suggested that the lack of a reducing environment during SARS-CoV-2 infection could favor the binding of the S-glycoprotein to ACE2.[32] Yet, it is unknown how the high levels of extracellular RONS affect the interaction between RBD and GRP78.

In this study, we used atomistic simulations to investigate the effect of Cys oxidation in RBD on its interaction with ACE2 and GRP78. For this purpose, we introduce the new binding site for the GRP78 receptor in our simulations. Our findings support the notion that Cys oxidation of RBD improves its interaction energy for ACE2, and it slightly increases it for GRP78. Overall, these findings highlight the role of RONS in the binding of the SARS-CoV-2 S-glycoprotein to host cell receptors and suggest an alternative mechanism by which RONS could modulate the entrance of viral particles into the cells.

2. COMPUTATIONAL DETAILS

2.1. Preparing the Initial Structure of the Proteins. Four specific regions of the RBD bound with the cell surface receptor were determined by Ibrahim et al., which contain four disulfide bonds[12] (see Figure 1). Specifically, these regions are region I (Cys_{336}−Cys_{361}, 26 residues), region II (Cys_{379}−Cys_{432}, 54 residues), region III (Cys_{391}−Cys_{525}, 135 residues), and region IV (Cys_{480}−Cys_{488}, 9 residues)[12] (Figure 1A). We have defined nonoverlapping regions, as introduced in Figure 1B, to refuse the recount of the value of nonbonded, salt bridge, and H-bonds for each region. These regions are region I (Cys_{336}−Cys_{361}), region II* (Cys_{379}−Leu_{390}), region II&III (Cys_{391}−Cys_{432}), region III* (Val_{433}−Pro_{479} and Tyr_{489}−Cys_{525}), and region IV (Cys_{480}−Cys_{488}). As shown in Figure 1B, region IV (purple) is not only cyclic but also surface-accessible and protrudes to the outer side of the S-glycoprotein, i.e., facing the target cell. Based on the crystal structure of RBD bound to ACE2 (PDB ID: 6M0J[33]) and the results of the molecular docking of RBD bound to GRP78,[12] we have identified that the most important amino acids in the interface of RBD and its receptor are located in region III* and especially in region IV. Because of the disulfide bond between Cys_{480} and Cys_{488} residues, region IV possesses a cyclic form, which can be destructed by breaking this disulfide bond as a result of Cys oxidation. Generally, if the distance of sulfur groups of two Cys residues in the protein structures is less than 2.04 Å,[34] they can be easily oxidized, making disulfide bonds. This process is completely reversible and can happen in normal conditions and at low levels of reactive oxygen species (ROS) in the cell surface.[35] Therefore, in the native conformation of RBD, ACE2, and GRP78, all Cys residues are considered in the oxidized form, as cystine.

The three-dimensional (3D) structure of the native RBD bound with ACE2 is available in the protein data bank (PDB ID: 6M0J).[33] Using the pydockWEB Web server,[36,37] we performed molecular docking to predict the binding site of the native RBD to GRP78 (i.e., RBD−GRP78 complex), as well as the native RBD to ACE2 (i.e., RBD−ACE2 complex). In the latter case, we compared the native RBD−ACE2 complex obtained by our docking with the existing complex from the PDB (see above) to validate the accuracy of our docking simulations. Moreover, the results of our docking on GRP78 and RBD were in agreement with the result of docking obtained by Ibrahim et al.[12] Because there is no Met residue in the native RBD structure, Cys is the next amino acid that can be easily oxidized. As mentioned before, the RBD domain contains eight Cys residues that form four disulfide bonds (i.e., four cystine residues). Cysteic acid (CYO) and cystine are the product of Cys oxidation by hydrogen peroxide (H_2O_2),[38] one of the RONS produced during oxidative stress in response to viral infections.[20] In general, intracellular RONS, such as H_2O_2, can oxidize 5% of the Cys residues of proteins to cysteic or Cys sulfenic acid,[39] and this effect is enhanced under oxidative stress.[28−31] Since all eight Cys residues of the RBD are in four cystine dimeric forms, oxidation of these residues leads to a next product, i.e., cysteic acid.

Hence, the oxidation of one cystine results in the breakage of the disulfide bond and the formation of two CYOs.[40] We oxidized two pairs of cystine (i.e., Cys_{379}−Cys_{432} and Cys_{480}−Cys_{488}) that are in contact with water molecules and located in the interfacial region of RBD with ACE2 or GRP78. Thus, after oxidation, two disulfide bonds were dissociated, thereby forming four CYOs.

To identify the partial charges of CYO residues, we first identified their protonation states in the physiological environment. The negative partial charge of CYO in the physiological condition is provided by the Drug bank,[41] which was considered in the preparation of CYO parameters in this study. In addition, experimental investigations on Cys oxidation also confirmed that the oxidation of Cys residues of proteins caused by ROS (such as H_2O_2) mostly results in negatively charged CYOs.[39]

To prepare the CHARMM-type force field parameters of negatively charged CYO (i.e., −1 *e*), we used a combination of Gaussian software[42] and the CHARMM general force field (CGenFF)[43] (see https://cgenff.parachem.org), similar to the procedure applied by van der Spoel et al.[44] To optimize and

https://doi.org/10.1021/acs.jcim.1c00853
J. Chem. Inf. Model. 2022, 62, 129−141

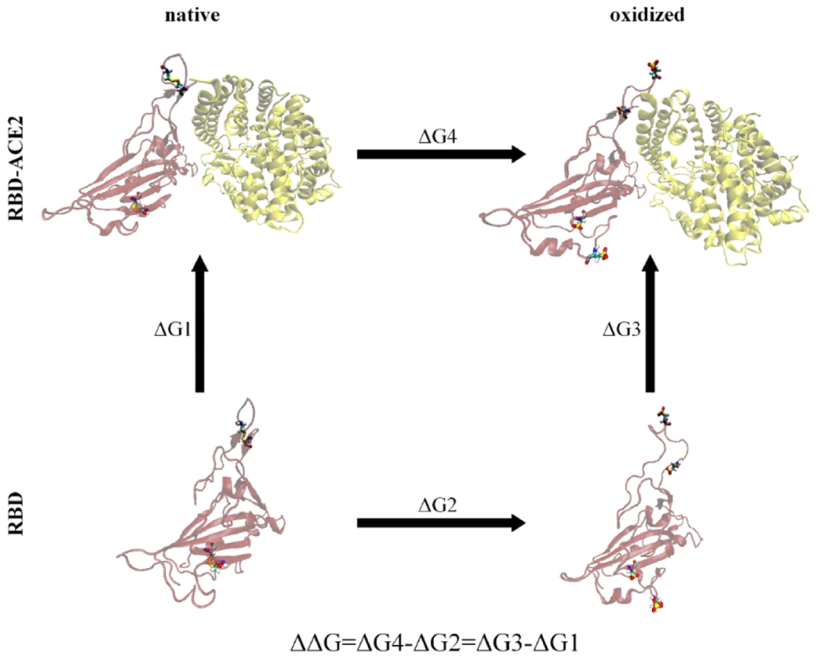

Figure 2. Schematic representation of a thermodynamic cycle to calculate changes in the free energy of RBD attachment to ACE2 upon Cys oxidation (ΔΔG). The left-hand side of the figure shows the attachment process of a native RBD and ACE2, with the attachment free energy ΔG1; the right-hand side of the figure shows the same attaching reaction but for an oxidized RBD−ACE2, resulting in the attachment free energy ΔG3. The process shown in the bottom row corresponds to the alchemical transformation of the native RBD into the oxidized one with the free energy difference ΔG2. The process in the top row relates to the same alchemical transformation but for the RBD−ACE2 complex, so the free energy difference between the two complexes via Cys oxidation is ΔG4.

generate partial charges of CYO, density functional theory (DFT), using the B3LYP functional with the standard 6-311G* basis set, was applied using Gaussian 16. Afterward, using the output from Gaussian 16, the topology files of CYO, compatible with the CHARMM36 force field, were constructed applying the CGenFF program.

2.2. Molecular Dynamics (MD) Simulation Protocols. MD simulations were performed using Gromacs 2020.2-MODIFIED software.[45] For all systems (i.e., native and oxidized RBDs in combination with native ACE2 and GRP78), the CHARMM36 force field was employed to describe the interatomic interactions. The initial systems were prepared by adding the TIP3P water model[46] into a box with the size of 13.66 × 13.66 × 13.66 nm^3 for the RBD−ACE2 and RBD−GRP78 complexes and 12.80 × 12.80 × 12.80 nm^3 for the RBD−GRP78 complex after removing the noninteracting tail of GRP78 (cf. Figure 4). The charges of all systems were neutralized by adding chlorine and sodium ions to the water in the simulation box. The energy minimization of the systems was performed using the steepest descent algorithm for 50 000 steps.

Four replicas were generated for each five complex system, i.e., (i) native RBD−ACE2, (ii) oxidized RBD−ACE2 (i.e., oxidized RBD bound to native ACE2), (iii) native RBD−GRP78 without removing the tail, and (iv) native and (v) oxidized RBD−GRP78 (i.e., oxidized RBD bound to native GRP78) with removing the tail, giving a total of 20 systems. The four replicas for each system applied different initial atomic velocities, using different random seeds. All systems were initially equilibrated in the isothermal (constant number of particles, volume, and temperature, NVT) ensemble at 310 K for 2 ns with a time step of 1 fs. Then, the isothermal−isobaric (constant number of particles, pressure, and temperature, NPT) ensemble at 310 K and 1 atm with a time step of 2 fs was applied until the root-mean-square deviations (RMSDs) of the proteins are relaxed (see the RMSD plots in Figures S1−S4 of the SI). The native RBD−ACE2 and oxidized RBD−ACE2 systems were equilibrated for 150 and 310 ns, respectively. The native RBD−GRP78 without removing its tail was equilibrated for 180 ns. Afterward, the native RBD−GRP78 and oxidized RBD−GRP78 systems were equilibrated for 280 and 410 ns, respectively (see the SI for more details). Equilibration of the systems was performed using the Nose−Hoover thermostat[47] with a coupling constant of 1 ns and the isotropic Parrinello−Rahman barostat[48] with a coupling constant and compressibility of 5 ns and 4.5 × 10^{-5} bar^{-1}, respectively. The Verlet list scheme was employed with the cutoff distance of 12 Å for both the electrostatic and van der Waals interactions. The particle mesh Ewald (PME) method was implemented to compute long-range electrostatic interactions[49,50] with long-range dispersion corrections for both energy and pressure. Periodic boundary conditions were applied to the systems in all three directions. Energy and structural analyses were carried out by applying the gmx energy tool of Gromacs and visual molecular dynamics (VMD) 1.9.4a43 software.[51]

To understand the reason for the increase in nonbonded interaction energy in the RBD−ACE2 complex after oxidation, we calculated the number of H-bonds and salt bridges formed between RBD and ACE2 before and after oxidation, using VMD software.[51] Following Debiec et al., we selected 3.5 and 4.5 Å for the formation and dissociation distances of the salt bridges, respectively.[52] Moreover, for the cutoff distance of the H-bond formation, we used 3 Å,[53] and the angle cutoff of D−H−A was equal to 20°. Note that we calculated the number of H-bonds and salt bridges by dividing the total number of H-

https://doi.org/10.1021/acs.jcim.1c00853
J. Chem. Inf. Model. 2022, 62, 129−141

bonds by the total number of MD frames (with an abundance of more than 10% in all frames), using the last 100 ns of MD simulations.

To find the best position of the interface of GRP78 and RBD in the complex, MD simulations were performed on the system initiated from the molecular docking. After equilibrating all four replicas of the native RBD−GRP78 system, the nonbonded interaction energy between RBD and GRP78 was calculated using the last 80 ns of MD simulations. Among all equilibrated replicas, the most stable one was chosen as the initial structure in our further simulations with the native and oxidized RBD−GRP78 complexes (i.e., RBD−GRP78 with the removed tail). Hence, to reduce the size of the simulation box (to speed up the simulations), the noninteracting tail of GRP78 was removed from the complex, and after energy minimization, four replicas of the native and oxidized RBD−GRP78 were generated.

2.3. Oxidation Free Energy Calculation. Alchemical mutation of the RBD structure (i.e., mutation of Cys_{379}, Cys_{432}, Cys_{480}, and Cys_{488} to cysteic acid) was applied to compute the free energy changes during the transformation of native RBD−ACE2 to the oxidized one and vice versa. Similar to the method used in refs 54 and 55, the hybrid protein structures and topology setup were designed for the native RBD−ACE2, oxidized RBD−ACE2, native RBD alone, and oxidized RBD alone. For each system, four replicas were prepared. The final frames of equilibrium MD trajectories were used as an initial structure for slow-growth free energy simulation.[56] In the slow-growth free energy simulation between the initial (state A) and final (state B) states, the system is always in thermodynamic quasi-equilibrium. This reversible process applies small changes during the transformation, which are very slow. The coupling parameter λ is used to drive the process, which is started at $\lambda = 0$ and finished at $\lambda = 1$. This parameter is constantly modified at each time step. The work on the system is obtained by integrating the energetic cost for modifying the system and is computed by

$$W(\tau) = \int_{\lambda=0}^{\lambda=1} \frac{\partial H(x, v, \lambda)}{\partial \lambda} \, d\lambda \quad (1)$$

where H is the Hamiltonian of the system. The initial and final states of the system and the path connecting them are shown in Figure 2. The initial states are the native and oxidized RBDs, which are individually solvated in the water without any interaction with ACE2, and the final states are the native and oxidized RBDs after interacting with ACE2. The defined cycle in Figure 2 shows the path between the native structures transforming into the oxidized one. The free energy difference of the RBD and ACE2 attraction upon Cys oxidation (ΔGG) is retrieved by following both the physical paths of attaching the native and oxidized RBDs to ACE2 (ΔG3 − ΔG1) and the alchemical paths of Cys oxidation of the RBD in the RBD alone and the RBD−ACE2 complex system (ΔG4 − ΔG2). The free energy difference ΔGG is calculated from the difference between ΔG2 and ΔG4, which have less computational cost and are computed here.

Sixteen initial structures were prepared for the slow-growth free energy simulation (i.e., native RBD−ACE2, oxidized RBD−ACE2, native RBD alone, and oxidized RBD alone, four replicas for each). All initial structures were initially in state A ($\lambda = 0$); then, by changing the λ value very smoothly, they transformed to state B ($\lambda = 1$). Therefore, the native ones converted to oxidized ones and vice versa. The simulation parameters were similar to the conventional MD runs, except that new flags were added in the mdp files for applying the free energy. Hence, the free energy calculation flag was switched on and the initial lambda was chosen as zero. The soft-core potential was used for Coulombic and van der Waals interactions with the values of $\alpha = 0.3$ and $\sigma = 0.25$, and the soft-core power was equal to 1. Transforming from the initial state to the final one was done slowly within 10 ns. The number of steps was equal to 5×10^6. Therefore, λ was changed smoothly from $\lambda = 0$ to 1 and $\Delta\lambda$ was equal to 2×10^{-7} $\left(\Delta\lambda = \frac{1}{5 \times 10^6} = 2 \times 10^{-7}\right)$. To extract the energy values, the gmx analyze-integrate tool of GROMACS was applied for both forward and backward transitions in each structure.

3. RESULTS AND DISCUSSION

3.1. Quality of the Chosen Structures Using Molecular Docking. The first RBD−ACE2 complex with the highest interaction energy (−44.646 kJ/mol) obtained from our docking simulations is not accessible to the RBD (see the cyan circle in Figure 3). Nevertheless, this complex cannot be considered in our simulations. The reason is that, under physiological conditions, ACE2 is decorated by glycans in the RBD−ACE2 interface of this complex, which were not taken into account on the molecular docking; hence, this complex cannot be accepted. The second RBD−ACE2 complex with the highest interaction energy (−35.532 kJ/mol) is fully compatible with the crystal structure of the RBD−ACE2 complex (PDB ID: 6M0J[33]). Thus, the molecular docking used in this study is sufficient to propose an initial GRP78−RBD complex for our molecular dynamics (MD) simulations.

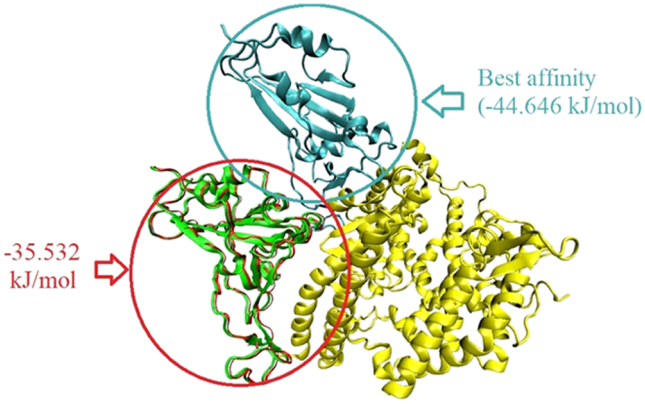

Figure 3. Superimposed structures of the crystal structure (green and yellow) and the molecular docking (red and yellow) of the RBD−ACE2 complex, representing the high compatibility between them. ACE2 is shown in yellow. The highest interaction energy between RBD and ACE2 (−44.646 kJ/mol) belongs to the complex where the ACE2 interface is not accessible for RBD binding (see the cyan circle). Note that the cyan and red circles, respectively, show the first and second positions of RBD with the highest affinity to ACE2, obtained from our docking simulations.

In the case of the RBD−GRP78 complex, we chose the crystal structures of the RBD domain (PDB ID: 6M0J[33]) and GRP78 (PDB ID: 5E84[57]) as a ligand and the protein, respectively. The molecular docking results with the highest interaction energy (−41.942 kJ/mol) showed that region III*, and specifically region IV, could bind to SBDβ and ATP

https://doi.org/10.1021/acs.jcim.1c00853
J. Chem. Inf. Model. 2022, 62, 129−141

binding domain (ABD) (or nucleotide binding domain NBD) (NBD/ABD domains) of GRP78 (see Figure 4).

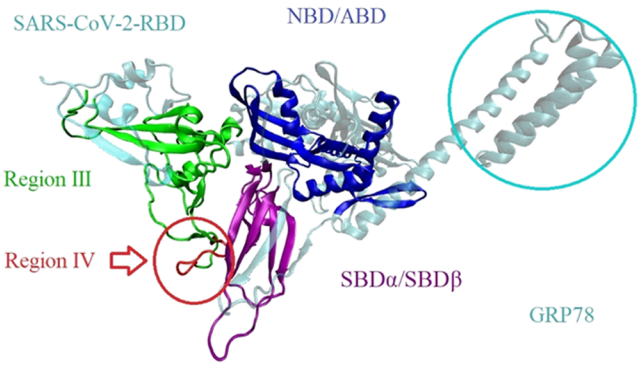

Figure 4. Results of the molecular docking for the RBD−GRP78 complex. Region III (green) and region IV (indicated by the red circle) of the RBD as well as SBDα/SBDβ (purple) and NBD/ABD (dark blue) domains of the GRP78 are represented here. The rest of the protein structures are shown by the pale-cyan color. The light-cyan circle indicates the position of the tail of GRP78 located inside the membrane. This tail is excluded in our further MD simulations (see details below).

3.2. Secondary Structural Analysis. The secondary structure analysis of the RBD before and after oxidation is shown in Table 1. As is clear, the oxidation of Cys residues to CYOs, which results in dissociation of the disulfide bridges and the repulsive interaction between negatively charged CYOs, destroyed some parts of the RBD structure, especially some of its β-sheets, and converted them to the coil structures (see also Figure 5).

3.3. Interaction Energy between SARS-CoV-2 RBD and ACE2. The nonbonded (i.e., Coulomb + van der Waals) interaction energies of the RBD and its various regions with ACE2, before and after oxidation of RBD, are shown in Tables 2 and 3. After oxidation of Cys_{379}, Cys_{432}, Cys_{480}, and Cys_{488} to CYO residues, the interaction energy between RBD and ACE2 became more negative, which indicates that Cys oxidation increases the attraction between RBD and ACE2 (Table 2). Table 3 shows the strongest interaction between region III* of RBD and ACE2, which became even stronger after oxidation, although no Cys oxidation takes place in this region. The reduction in nonbonded energy between region IV of RBD and ACE2 as well as the higher root-mean-square fluctuation (RMSF) of the amino acid residues in this region after oxidation (see Figure S5) demonstrated the partial separation of region IV from ACE2. This separation as well as conformational changes in region IV, hence, affected the interaction of region III* with ACE2, thereby increasing the nonbonded energy between them (Table 3).

The interaction energies of the amino acid residues of regions III* and IV of RBD with ACE2 in the native and oxidized complexes are summarized in Tables 4 and 5, respectively. The importance of region III* is because Cys oxidation did not happen there, but had the most contribution

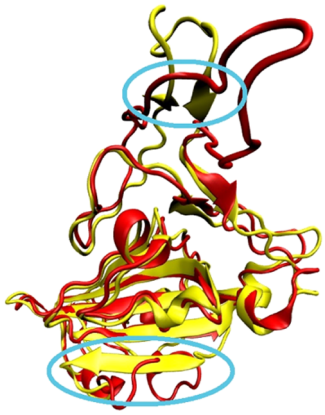

Figure 5. Superimposed structure of the native (yellow) and oxidized (red) RBDs displayed in the new-cartoon representation. The light-blue ellipses show the positions of the β-sheets in the native RBD, which are destroyed after Cys oxidation.

Table 2. Coulomb, van der Waals, and Total Nonbonded Interaction Energies between RBD and ACE2 for the Native and Oxidized Complexes

	Coulomb energy (kJ/mol)	van der Waals energy (kJ/mol)	total energy (kJ/mol)
native	−325 ± 15	−229 ± 7	−554 ± 21
oxidized	−409 ± 4	−300 ± 17	−709 ± 14

in the difference of nonbonded energy between native and oxidized complexes. As is shown in Table 4, for most important amino acid residues of region III*, the attractive interactions with ACE2 were increased after Cys oxidation, especially for Lys_{458}−ACE2, Pro_{479}−ACE2, Gln_{493}−ACE2, Gln_{498}−ACE2, Thr_{500}−ACE2, and Tyr_{505}−ACE2, while the attractive interaction of Ala_{475}−ACE2 was significantly decreased. Based on the literature,[58,59] Ala_{475} is one of the important amino acids of RBD that plays a crucial role in ACE2 attachment. Conformational changes of the RBD−ACE2 complex after Cys oxidation reduced the attractive interaction of Ala_{475} with ACE2, but this reduction was not enough to affect the total nonbonded energy of region III* and other residues retrieved it. Furthermore, studies in the literature[58,59] showed that Phe_{486} and Asn_{487} of region IV are important for RBD−ACE2 attachment. As is clear from Table 5, Cys oxidation significantly reduced the nonbonded energy of these two mentioned residues and Glu_{484} with ACE2. The reduction in nonbonded energy between these residues and ACE2 allowed them to move more freely.

Thus, our simulation results of the nonbonded interaction energies indicate that the binding of RBD to ACE2 becomes stronger after oxidation of RBD, compared to that of the native RBD−ACE2 complex.

Tables 6 and 7 show the total number of H-bonds and salt bridges formed between each region of the RBD and ACE2, respectively. Investigation of the amino acid residues of region IV showed that the most important H-bonds were observed

Table 1. Secondary Structure Analysis of the Native and Oxidized RBD

	coil (%)	β-sheet/β-bridge (%)	bend (%)	turn (%)	α, 5, and 3 helixes (%)
native RBD	32.7 ± 0.5	28.0 ± 0.1	13.5 ± 0.6	11.5 ± 0.3	14.0 ± 0.4
oxidized RBD	37.7 ± 0.6	23.0 ± 0.4	13.2 ± 0.2	11.0 ± 0.1	14.5 ± 0.5

https://doi.org/10.1021/acs.jcim.1c00853
J. Chem. Inf. Model. 2022, 62, 129−141

Table 3. Total Nonbonded Interaction Energy between Regions of the RBD (i.e., I, II*, II&III, III*, and IV) and ACE2 for the Native and Oxidized Complexes

	region I-ACE2 (kJ/mol)	region II*-ACE2 (kJ/mol)	region II&III-ACE2 (kJ/mol)	region III*-ACE2 (kJ/mol)	region IV-ACE2 (kJ/mol)
native	$<10^{-2}$	$<10^{-2}$	−84 ± 7	−339 ± 14	−130 ± 9
oxidized	$<10^{-2}$	$<10^{-2}$	−94 ± 2	−502 ± 15	−113 ± 9

Table 4. Nonbonded Interaction Energies between Amino Acid Residues of Region III* of RBD and ACE2 for the Native and Oxidized Complexes[a]

interaction	native (kJ/mol)	oxidized (kJ/mol)
Tyr_{499}–ACE2	−10.3 ± 1.7	−12.2 ± 3.3
Leu_{455}–ACE2	−10.2 ± 0.1	−11.7 ± 0.6
Phe_{456}–ACE2	−21.2 ± 0.2	−19.3 ± 1.2
Lys_{458}–ACE2	−0.6 ± 0.7	−13.5 ± 4.2
Tyr_{473}–ACE2	−7.0 ± 0.3	−11.7 ± 3.6
Ala_{475}–ACE2	−30.3 ± 0.8	−10.7 ± 1.2
Gly_{476}–ACE2	−11.5 ± 0.7	−10.1 ± 1.2
Ser_{477}–ACE2	−4.9 ± 0.5	−11.8 ± 2.1
Pro_{479}–ACE2	−0.008 ± 0.001	−11.9 ± 3.2
Tyr_{489}–ACE2	−21.9 ± 0.2	−25.1 ± 3.1
Gln_{493}–ACE2	−29.9 ± 2.1	−46.8 ± 6.1
Gln_{496}–ACE2	−7.1 ± 0.8	−22.3 ± 7.2
Gln_{498}–ACE2	−13.8 ± 1.3	−46.7 ± 13.1
Thr_{500}–ACE2	−37.4 ± 7.7	−44.6 ± 5.5
Asn_{501}–ACE2	−53.9 ± 5.3	−58.2 ± 2.3
Gly_{502}–ACE2	−20.2 ± 0.6	−22.9 ± 0.7
Tyr_{505}–ACE2	−34.2 ± 1.6	−41.2 ± 7.2

[a]The residues with nonbonded energy absolute values of less than 10 kJ/mol for native and oxidized complexes are not shown here.

Table 5. Nonbonded Interaction Energies between Amino Acid Residues of Region IV of RBD and ACE2 for the Native and Oxidized Complexes[a]

interaction	native (kJ/mol)	oxidized (kJ/mol)
Glu_{484}–ACE2	−54.8 ± 10.6	−1.4 ± 0.4
Phe_{486}–ACE2	−30.1 ± 0.6	−11.8 ± 6.5
Asn_{487}–ACE2	−42.5 ± 1.5	−19.3 ± 4.5
Cys_{488}–ACE2	−1.7 ± 0.1	−58.8 ± 21.4

[a]The residues with nonbonded energy absolute values of less than 10 kJ/mol for native and oxidized complexes are not shown here.

between two pairs, i.e., Glu_{484}–Lys_{31} and Asn_{487}–Tyr_{83} (see Table S2). Among them, a salt bridge was also observed between Glu_{484} and Lys_{31} (see Table S2). All mentioned H-bonds and the observed salt bridge were destroyed after oxidation of RBD (see Table S3). The mostly observed H-bonds between amino acid residues of region III* and ACE2 were formed between three pairs, Gly_{502}–Lys_{353}, Thr_{500}–Asp_{335}, and Ala_{475}–Ser_{19} (see Table S2). After oxidation, the number of amino acid residues of region III*, which could form H-bonds, was even increased due to conformational changes. These pairs are Gly_{502}–Lys_{353}, Thr_{500}–Asp_{355}, Gln_{498}–Lys_{353}, Gln_{493}–Gln_{35}, Tyr_{505}–Glu_{37}, and Gly_{496}–Lys_{353} (see Table S3). The results showed that Lys_{353} of ACE2 is the most important residue for H-bonds with three amino acid residues of region III*. Note that the importance of Lys_{353} in the binding interaction of ACE2 with RBD was also mentioned in ref 60. The number of salt bridges of region II&III is almost the same after oxidation (i.e., within the error), while the number of H-bonds decreased after oxidation, both of which are only between Lys_{417}–Asp_{30} (see Tables S2 and S3).

Thus, after oxidation of Cys residues in RBD, some of the H-bonds and salt bridges between the regions of RBD and ACE2 were formed and/or broken, which eventually resulted in an increase of the nonbonded interaction energy between RBD and ACE2, making their interaction stronger.

The value of free energy differences between the native and oxidized complexes ΔΔG according to ΔG4 − ΔG2 (see thermodynamic cycle in Figure 2) became more negative and equal to −55.1 ± 31.5 kJ/mol, showing that the oxidized RBD–ACE2 complex is more stable than the native one. The result was obtained from averaging over all forward and backward simulation runs of all 16 simulations. The calculated free energy was in agreement with the result of nonbonding energy calculations, showing that the oxidized RBD–ACE2 complex is more stable than the native one and the binding affinity between oxidized RBD and ACE2 is greater than the native complex.

3.4. Interaction Energy between SARS-CoV-2 RBD and GRP78. To investigate the effect of Cys oxidation in RBD on its interaction with the GRP78 receptor protein, we extracted the initial structure of the RBD–GRP78 complex from our molecular docking simulation. As mentioned in Section 2, four replicas with different initial atomic velocities were generated for the RBD–GRP78 complex and subsequently equilibrated using the MD simulations. The results of the trajectories of the equilibrated replicas were compared to each other. We found that out of the four replicas, RBD and GRP78 were separated in a single case, and the RBD binding position to GRP78 was changed in the case of another replica, which we call replica-2. Figure 6 illustrates the superimposed structures of replica-2, i.e., obtained by molecular docking (nonequilibrated) and equilibrated with MD simulation. It is clear that the equilibrated complex (shown in green and yellow) had a new interface for RBD and GRP78, which was completely different from the initial interface obtained by molecular docking (blue and red colors).

Table 6. Number of H-Bonds Formed between Each Region of the Native/Oxidized RBD and ACE2[a]

	region I-ACE2	region II*-ACE2	region II&III-ACE2	region III*-ACE2	region IV-ACE2
native			0.50 ± 0.01	0.85 ± 0.09	0.53 ± 0.05
oxidized			0.38 ± 0.05	1.29 ± 0.10	

[a]Values are obtained by dividing the total number of H-bonds by the total number of MD frames (with the abundance of more than 10% in all frames), using the last 100 ns of the MD simulation.

https://doi.org/10.1021/acs.jcim.1c00853
J. Chem. Inf. Model. 2022, 62, 129−141

Table 7. Number of Salt Bridges Formed between Each Region of the Native/Oxidized RBD and ACE2[a]

	region I-ACE2	region II*-ACE2	region II&III-ACE2	region III*-ACE2	region IV-ACE2
native			0.80 ± 0.06		0.32 ± 0.08
oxidized			0.89 ± 0.06		

[a]Values are obtained by dividing the total number of salt bridges by the total number of MD frames (with the abundance of more than 10% in all frames), using the last 100 ns of the MD simulation.

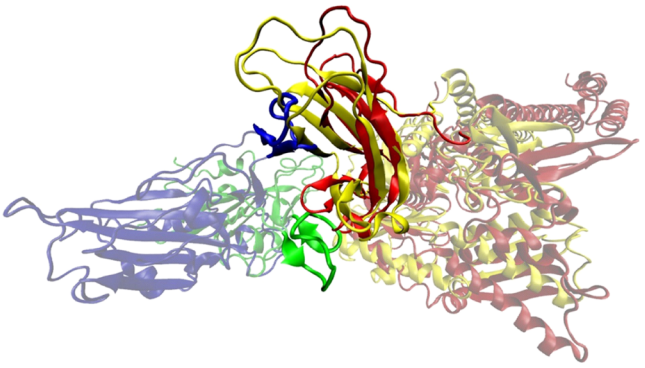

Figure 6. Superimposed structures of the initial (i.e., nonequilibrated) RBD−GRP78 complex (blue/red) extracted from the molecular docking and its equilibrated conformation (green/yellow) of replica-2. Interacting parts of RBD (blue or green) and GRP78 (red or yellow) are shown bright, while the other parts are in pale colors.

The results indicate that replica-2 of the RBD−GRP78 complex was energetically more stable than the other two replicas (see Tables 8 and 9). Moreover, the smaller RMSD fluctuations indicate more structural stability of the RBD−GRP78 complex in replica-2, compared to the other replicas (see Figure S3A).

Table 8. Coulomb, van der Waals, and Total Nonbonded Interaction Energies between RBD and GRP78 for Three Replicas

	Coulomb energy (kJ/mol)	van der Waals energy (kJ/mol)	total nonbonded energy (kJ/mol)
replica-1	−100 ± 3	−155 ± 12	−255 ± 15
replica-2	−235 ± 21	−163 ± 9	−398 ± 30
replica-3	−83 ± 7	−111 ± 5	−194 ± 12

Thus, replica-2 was selected for the creation of initial structures of the native and oxidized RBD−GRP78 complexes, i.e., four replicas with removed tails (see the previous section for details) for each complex, used in our further MD simulations. In the case of the native RBD−GRP78 system, all four replicas remained stable after equilibration (see RMSDs in Figure S4A), showing that the configuration is favorable. Therefore, we can conclude that the obtained interface of the RBD−GRP78 complex is more probable compared with the one that was proposed by our molecular docking. Moreover, in the case of the oxidized RBD−GRP78 system, the RMSDs were higher than those in the native system, indicating the higher flexibility of the oxidized system (see Figure S4B). The latter can make the interaction of RBD with GRP78 weaker, i.e., decreasing the nonbonded interaction energy.

The averaged Coulomb, van der Waals, and total nonbonded interaction energies of the native and oxidized RBD−GRP78 complexes are shown in Table 10. The total nonbonded interaction energy slightly increases after oxidation of RBD, although the values are close (i.e., within the errors). After equilibration of the four replicas of the oxidized RBD−GRP78 complex, in one replica, GRP78 and oxidized RBD separated from each other, whereas in the other replicas, the interfaces of GRP78 and RBD were switched to the other parts of the proteins (i.e., from regions III* and IV to region I; see below). In fact, Cys oxidation in the early steps of the MD simulation causes separation between RBD and GRP78. After that, as the simulation time was increased, GRP78 can find a new binding domain in region I of RBD to attach. These structural changes are visible as jumps of RMSD in MD simulations in all of the replicas (see Figure S4B). After RBD oxidation, the strongest interaction was obtained between GRP78 and region I of RBD (see Table 11), which is not in a favorable position in the presence of the rest of the SARS-CoV-2 S protein. In fact, GRP78 cannot access this domain, unless by overlapping with the rest of the SARS-CoV-2 S protein. It is also obvious from Table 11 that the oxidation of RBD led to a decrease of the nonbonded interaction energies between regions II&III, III*, and IV and GRP78. In the native complex, the nonbonded interaction energy between GRP78 and region IV was the highest one. The hydrophobic amino acid residues of region IV and its cyclic and protruded form made this region suitable to bind with the GRP78.[12] As is clear from Table 11, after Cys oxidation, the nonbonded interaction energy between GRP78 and region IV predominantly reduced and these two structures separated from each other and the binding site of the RBD to the GRP78 switched to region I, thereby making its interaction the strongest with GRP78.

Table 10. Coulomb, van der Waals, and Total Nonbonded Interaction Energies between RBD and GRP78 for the Native and Oxidized Systems

	Coulomb energy (kJ/mol)	van der Waals energy (kJ/mol)	total energy (kJ/mol)
native	−302 ± 45	−170 ± 15	−473 ± 60
oxidized	−371 ± 42	−110 ± 25	−481 ± 53

Table 9. Total Nonbonded Interaction Energy between Each Region of the RBD (i.e., I, II*, II&III, III*, and IV) and GRP78 for Three Replicas

	region I-GRP78	region II*-GRP78	region II&III-GRP78	region III*-GRP78	region IV-GRP78
replica-1	$<10^{-5}$	0	−0.13 ± 0.06	−89 ± 10	−166 ± 12
replica-2	$<10^{-5}$	0	−1.5 ± 0.6	−162 ± 11	−234 ± 23
replica-3	$<10^{-5}$	0	−18.4 ± 0.2	−117 ± 7	−59 ± 10

https://doi.org/10.1021/acs.jcim.1c00853
J. Chem. Inf. Model. 2022, 62, 129−141

Table 11. Nonbonded Interaction Energies between Regions of the RBD (i.e., I, II*, II&III, III*, and IV) and GRP78 for the Native and Oxidized Systems

	region I-GRP78 (kJ/mol)	region II*-GRP78 (kJ/mol)	region II&III-GRP78 (kJ/mol)	region III*-GRP78 (kJ/mol)	region IV-GRP78 (kJ/mol)
native	$<10^{-4}$	$<10^{-6}$	−46 ± 28	−195 ± 45	−231 ± 21
oxidized	−261 ± 46	$<10^{-6}$	−0.4 ± 0.3	−199 ± 23	−21 ± 19

Figure 7 illustrates a snapshot of the MD trajectory of the equilibrated RBD−GRP78 complex in the oxidized form.

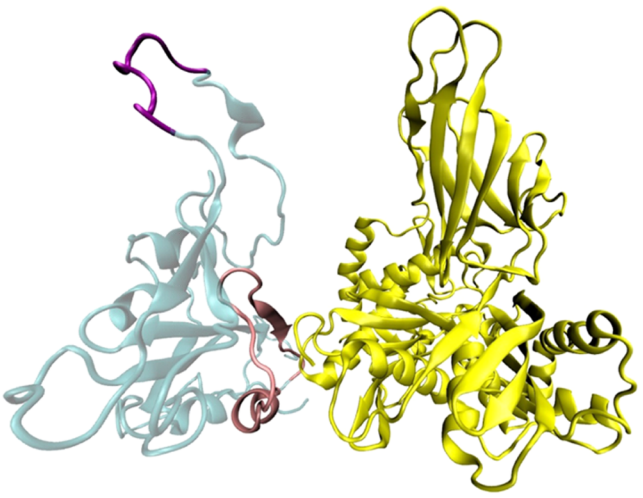

Figure 7. New-cartoon representation of the oxidized RBD−GRP78 (cyan/yellow) complex. Region I (pink) located below has the most important interaction with GRP78. Region IV (purple) located above is separated from GRP78 after Cys oxidation in RBD. The figure is taken as a snapshot from the equilibration trajectories of the oxidized RBD−GRP78 system.

Region I (pink) is the most important part with the strongest interaction with GRP78. Moreover, the RMSF of all RBD and some GRP78 amino acid residues increased after Cys oxidation, meaning that oxidation caused the separation of RBD and GRP78 from each other, which allowed them to fluctuate more compared to the native complex (see Figure S6).

Thus, our simulation results of the nonbonded interaction energies indicate that the binding of RBD to GRP78 did not significantly change after oxidation of RBD, compared to that of the RBD−ACE2 complex. However, most of this interaction energy in oxidized RBD−GRP78 comes from interactions between region I of RBD and GRP78, which is not accessible if the rest of the SARS-CoV-2 S protein is considered. Therefore, we can conclude that the interaction energy between accessible domains of RBD and GRP78 significantly reduces after RBD oxidation.

We calculated the number of H-bonds and salt bridges (i.e., with the abundance of more than 10%) formed between RBD and GRP78 before and after oxidation, which are presented in Tables 12 and 13, respectively. Analysis of the H-bond and salt bridge formation in the native and oxidized conformations shows that the number of H-bonds and salt bridges was reduced after oxidation.

After oxidation of RBD, due to conformational changes, the H-bonds and salt bridges in the oxidized RBD−GRP78 complex were destroyed and new ones were formed (compared to the native system), which are mostly between region I and GRP78. The most specific H-bonds with the abundancy of more than 10% were formed between regions III* and IV of RBD and GRP78 in the native structure (see Table S4). In region IV, Glu_{484} is the only amino acid that formed H-bonds with three residues (i.e., Lys_{424}, Lys_{412}, and Thr_{411}) of GRP78. In region III*, two amino acids Gly_{477} and Tyr_{505} formed H-bonds with Pro_{421} and Glu_{220} of GRP78, respectively (see Table S4). After oxidation of RBD, these H-bonds of regions III* and IV were dissociated and three new H-bonds were formed between amino acid residues of regions I and III* and GRP78. These three H-bonds are Arg_{466}−Asp_{3}, Lys_{444}−Asp_{390}, and Glu_{340}−Lys_{140} (see Table S5). The first two pairs are formed between residues of region III* and GRP78, and the latter one is formed between region I and GRP78. Among all mentioned pairs, two pairs (Glu_{484}−Lys_{424} and Glu_{484}−Lys_{412}) in the native structure and two pairs (Lys_{444}−Asp_{390} and Glu_{340}−Lys_{140}) in the oxidized structure formed salt bridges.

These changes in H-bonds and salt bridges after oxidation of RBD might probably result in separation of these two proteins from each other (as was the case in one replica out of four; see above), eventually leading to an elimination of the effect of the GRP78 receptor on SARS-CoV-2 infection.

Taken together, these results demonstrate that although Cys oxidation does not change the interaction energy of oxidized RBD and GRP78, it is quite effective in altering the interface of oxidized RBD and GRP78, which is not desirable in the overall structure of the SARS-CoV-2 S protein. Therefore, oxidation of Cys residues of RBD strengthens the attachment of RBD to ACE2 and attenuates the binding between RBD and GRP78.

3.5. Discussion. Although initially RONS are produced to counteract viral infections, several viruses have found ways to benefit from this adverse environment. In SARS-CoV-2 particularly, this state of oxidative stress is considered key for the pathogenesis of the disease.[20] In this study, we describe how oxidation of SARS-CoV-2 RBD alters its interaction with two main receptors in host cells, ACE2 and GRP78.

Our MD simulations show that the interaction energy between RBD and ACE2 is enhanced when RBD is oxidized. This is in agreement with the recent publication of Hati et al.[32] The authors also applied MD simulations to investigate the

Table 12. Number of H-Bonds Formed between Each Region of the Native/Oxidized RBD and GRP78[a]6

	region I-GRP78	region II*-GRP78	region II&III-GRP78	region III*-GRP78	region IV-GRP78
native				0.27 ± 0.10	0.62 ± 0.09
oxidized	0.17 ± 0.11			0.41 ± 0.25	

[a]Values are obtained in the same way as mentioned in Table 6.

https://doi.org/10.1021/acs.jcim.1c00853
J. Chem. Inf. Model. 2022, 62, 129−141

Table 13. Number of Salt Bridges Formed between Each Region of the Native/Oxidized RBD and GRP78[a]7

	region I-GRP78	region II*-GRP78	region II&III-GRP78	region III*-GRP78	region IV-GRP78
native					0.58 ± 0.18
oxidized	0.29 ± 0.08			0.20 ± 0.09	

[a]Values are obtained in the same way as mentioned in Table 7.

effect of Cys oxidation (i.e., converting to the cystine form) of both RBD and ACE2 on their interaction energies and found that Cys oxidation to cystine in RBD increased its interaction energy to ACE2, compared to the reduced form. Due to the reversible process of cystine formation and reduction under physiological conditions,[35] Cys residues of both RBD and receptors can be easily oxidized to cystine. Excessive levels of RONS as a result of viral infection can oxidize these residues to cysteic acid, the irreversible product of Cys oxidation.[61]

In our study, the native structural complexes of RBD contained Cys in the form of cystine, while in the oxidized structural complexes, the cystine residues of RBD were irreversibly oxidized to cysteic acid. As receptors, we considered the native structural complexes, which are biologically functional. Moreover, when extracellular reactive species are produced during infection, only the oxidation of cystine residues of RBD to cysteic acid is possible. The comparative interaction energy of native and oxidized RBD−ACE2 shows that RBD oxidation strengthens the attraction of RBD and ACE2. In other words, oxidation of the thiol group of RBD and ACE2 (in any stage of oxidation) increases the interaction energy of RBD and ACE2, which is beneficial for the viral infection. In contrast, Cys oxidation in the oxidized RBD−GRP78 complex changes the interface of RBD and GRP78, introducing a new one between region I of RBD and GRP78. Considering the nonaccessibility of this new interface between RBD and GRP78, after separation of GRP78 from regions IV and III* of oxidized RBD (i.e., the regions of RBD were initially attached with GRP78), the complex will separate. Furthermore, the H-bond and salt bridge formation between amino acid residues of RBD and both receptors in the native and oxidized forms revealed that Lys_{353} of ACE2, which plays an important role in binding of native RBD and ACE2,[60] was more important in the oxidized RBD−ACE2 complex. In the native RBD−ACE2 complex, the Lys_{353} residue had only a H-bond with Gly_{502}, but in oxidized RBD−ACE2, it formed H-bonds with three residues, i.e., Gly_{502}, Gln_{498}, and Gly_{496}. Moreover, Glu_{484} is the only amino acid of region IV of the native RBD that could form H-bonds with three amino acids of GRP78, i.e., Thr_{411}, Lys_{412}, and Lys_{424}. It should be noted that the last two residues could also form salt bridges with Glu_{484}. All of these H-bonds and salt bridges between region IV and GRP78 were destroyed after oxidation of RBD.

To the best of our knowledge, this is the first time that the effect of this stage of Cys oxidation (i.e., to cysteic acid) on binding of the RBD is investigated. The effect of oxidation of Tyr_{449}, Tyr_{453}, Asn_{487}, and Gln_{498} of RBD on binding to ACE2 using MD simulation has been previously reported in the literature,[62] showing that the oxidation of Tyr, Asn, and Gln to 3,4-dihydroxyphenylalanine, 3-hydroxyasparagine, and 4-hydroxyglutamine, respectively, reduced the interaction energy of RBD and ACE2. This stage of oxidation could occur if the RBD is exposed to a high level of ROS.[28,30] In addition, the oxidation and nitration of SARS-CoV-2 RBD is experimentally investigated using external sources of reactive species, such as cold atmospheric plasma[63] and electrochemical oxidation.[64] Guo et al. showed that cold atmospheric plasma can be effective in the destruction of RBD and eventually its separation from ACE2.[63] Oxidation and nitration of Tyr and Trp of RBD to 3-nitrotyrosine and 6-nitrotryptophan, respectively, by $ONOO^-$ and $O_2^{\bullet -}$ were proposed as a reason for the aggregation and fragmentation of RBD. Furthermore, Tu et al. showed that the electrochemical oxidation of RBD mostly decomposes the aromatic residues of RBD (i.e., Tyr, Trp, and Phe).[64] It is important to mention that the fragmentation and decomposition of RBD cannot be investigated by conventional MD simulations due to the inability of these methods to form and break bonds. In addition, an excessive level of RONS is needed for oxidation and nitration of aromatic residues, which are not considered in our study. While the focus of the mentioned publications is on the alteration of RBD and the change of its binding to ACE2, our study in addition shows for the first time the effect of oxidation of RBD on GRP78 binding, in addition to presentation of the new interface of RBD and GRP78.

SARS-CoV-2 manipulates the cell machinery to destabilize the redox state, which creates a deficiency in antioxidants and favors viral replication.[20] Our findings suggest another way in which oxidative stress created by SARS-CoV-2 could modulate its entry to cells: while oxidation of RBD allows it to bind more efficiently to ACE2, it destabilizes RBD binding to GRP78. GRP78 has been identified as a novel regulator of ACE2 cell surface expression.[65] Even more, GRP78 can directly bind to ACE2 and act as a scaffold for RBD and ACE2 interaction on the cell surface.[65] Thus, it is possible that in a state of oxidative stress, GRP78 ensures the availability and stability of ACE2 at the cell surface, but it does not directly bind to RBD. Nevertheless, oxidized RBD binds to ACE2 with a higher interaction energy, which could compensate for the lack of interaction with GRP78. We have taken into account the effect of the oxidative environment not only on RBD but also on ACE2 and GRP78, as our simulations were done using the oxidized form of both protein receptors. Thus, the complexes formed between RBD and ACE2 or GRP78 used in this study reflect the possible interactions in the highly oxidative environment created during infection. Yet, further studies to determine the stability and binding affinity of the ACE2−GRP78−RBD complex under oxidative stress are needed.

Our findings could help toward the development of novel therapies to target ACE2 and GRP78, as well as to modulate cellular redox pathways to restore the homeostasis in SARS-CoV-2 infections. This could be particularly relevant for the development of viral-like particles (VLPs) for SARS-CoV-2 infection. These self-assembled structures could present oxidized RBD proteins (with higher interaction energy) that compete with viral RBD for ACE2 and GRP78 binding sites, thus reducing viral replication in the host cells. VLPs with improved interaction energy for their receptors could also be used to deliver specific drugs into the cell upon cell fusion.

https://doi.org/10.1021/acs.jcim.1c00853
J. Chem. Inf. Model. 2022, 62, 129−141

4. CONCLUSIONS

In this study, we investigated the effect of oxidation of Cys residues (as the amino acid most prone to oxidation) in the receptor-binding domain (RBD) of SARS-CoV-2 (simply called RBD) on its binding with cell receptors ACE2 and GRP78. Our atomistic simulations reveal that after Cys oxidation of RBD, the nonbonded interaction energy between RBD and ACE2 increases by 155 ± 21 kJ/mol, thus strengthening the attraction between them. Oxidation results in a partial separation of region IV and ACE2 in the complex, which means that region III* could strongly bind to ACE2 and eventually enhance the attraction between RBD and ACE2. In contrast, Cys oxidation of RBD only causes a small increase in the nonbonded interaction energy between RBD and GRP78, but the difference (i.e., ∼8 ± 60 kJ/mol) does not have a significant effect in their interaction. However, it induces conformational changes that cause the separation of regions IV and III* from GRP78 and destabilize the RBD−GRP78 complex. In this scenario, the attractive interaction between region I of RBD and GRP78 is possible, which was not accessible before RBD oxidation. However, considering the whole structure of the S-glycoprotein, the interaction of region I of RBD and GRP78 would not be possible, and the RBD−GRP78 complex would separate. These findings could be interesting for new therapies that target ACE2 and GRP78, as well as to adjust cellular redox pathways to restore the homeostasis in SARS-CoV-2 infections.

■ ASSOCIATED CONTENT

Supporting Information

The Supporting Information is available free of charge at https://pubs.acs.org/doi/10.1021/acs.jcim.1c00853.

> Amino acids that are most susceptible to oxidation; RMSD and RMSF plots; number of most probable H-bonds and salt bridges between amino acid residues of the RBD and ACE2; averaged RMSF of amino acid residues of the RBD and GRP78 proteins; number of most probable H-bonds and salt bridges between amino acidresidues of the RBD and GRP78 (PDF)

■ AUTHOR INFORMATION

Corresponding Authors

Maryam Ghasemitarei − *Department of Physics, Sharif University of Technology, Tehran 14588-89694, Iran; Research Group PLASMANT, Department of Chemistry, University of Antwerp, B-2610 Antwerp, Belgium;* orcid.org/0000-0003-1954-2048; Email: qasemi.maryam.mamh@gmail.com

Mohammad Reza Ejtehadi − *Department of Physics, Sharif University of Technology, Tehran 14588-89694, Iran;* orcid.org/0000-0002-0515-0695; Email: ejtehadi@sharif.edu

Authors

Angela Privat-Maldonado − *Research Group PLASMANT, Department of Chemistry, University of Antwerp, B-2610 Antwerp, Belgium*

Maksudbek Yusupov − *Research Group PLASMANT, Department of Chemistry, University of Antwerp, B-2610 Antwerp, Belgium; Laboratory of Thermal Physics of Multiphase Systems, Arifov Institute of Ion-Plasma and Laser Technologies, Academy of Sciences of Uzbekistan, 100125 Tashkent, Uzbekistan;* orcid.org/0000-0003-4591-858X

Shadi Rahnama − *Institute for Nanoscience & Nanotechnology (INST), Sharif University of Technology, Tehran 14588-89694, Iran*

Annemie Bogaerts − *Research Group PLASMANT, Department of Chemistry, University of Antwerp, B-2610 Antwerp, Belgium;* orcid.org/0000-0001-9875-6460

Complete contact information is available at: https://pubs.acs.org/10.1021/acs.jcim.1c00853

Notes

The authors declare no competing financial interest.

We used the Gromacs 2020.2-MODIFIED suite for MD simulations and Gaussian 16 for partial charge calculation. Three-dimensional structures of proteins are extracted from https://www.rcsb.org/. We used the server https://cgenff.parachem.org to prepare the CHARMM-type force field parameters. The Web server https://life.bsc.es/pid/pydockweb/ was applied for molecular docking to predict the binding site of proteins. All analyses were obtained by Gromacs and VMD 1.9.4a43 software, and the graphs are plotted by Grace-5.1.25. Software, Web servers, and computational tools described in this paper are owned by their respective developers and copyright-holders.

■ ACKNOWLEDGMENTS

M.G. acknowledges financial support from the "National Elites Foundation" for supporting the first author while working on this project as a part of her postdoctoral program. M.Y. gratefully acknowledges financial support from the Research Foundation—Flanders (FWO), grant number 1200219N. The computational work was carried out using the Turing HPC infrastructure at the CalcUA core facility of the Universiteit Antwerpen (UA), a division of the Flemish Supercomputer Center VSC, funded by the Hercules Foundation, the Flemish Government (department EWI), and the UA. We thank the HPC of Sharif University of Technology in Iran and the University of Antwerp in Belgium. Finally, we are grateful to A. S. Mashayekh Esfehan for reading the manuscript carefully and the important and valuable comments on the manuscript.

■ REFERENCES

(1) https://www.worldometers.info/coronavirus/.

(2) Coronaviridae Study Group of the International Committee on Taxonomy of Viruses. The species Severe acute respiratory syndrome-related coronavirus: classifying 2019-nCoV and naming it SARS-CoV-2. *Nat. Microbiol.* **2020**, *5*, 536.

(3) https://www.who.int/.

(4) Chan, J. F.-W.; Yuan, S.; Kok, K.-H.; To, K. K.-W.; Chu, H.; Yang, J.; Xing, F.; Liu, J.; Yip, C. C.-Y.; Poon, R. W.-S.; et al. A familial cluster of pneumonia associated with the 2019 novel coronavirus indicating person-to-person transmission: a study of a family cluster. *Lancet* **2020**, *395*, 514−523.

(5) Ibrahim, I. M.; Abdelmalek, D. H.; Elfiky, A. A. GRP78: A cell's response to stress. *Life Sci.* **2019**, *226*, 156−163.

(6) Wrapp, D.; Wang, N.; Corbett, K. S.; Goldsmith, J. A.; Hsieh, C.-L.; Abiona, O.; Graham, B. S.; McLellan, J. S. Cryo-EM structure of the 2019-nCoV spike in the prefusion conformation. *Science* **2020**, *367*, 1260−1263.

(7) Wang, Q.; Zhang, Y.; Wu, L.; Niu, S.; Song, C.; Zhang, Z.; Lu, G.; Qiao, C.; Hu, Y.; Yuen, K.-Y.; et al. Structural and functional basis of SARS-CoV-2 entry by using human ACE2. *Cell* **2020**, *181*, 894.e9−904.e9.

(8) Kirchdoerfer, R. N.; Wang, N.; Pallesen, J.; Wrapp, D.; Turner, H. L.; Cottrell, C. A.; Corbett, K. S.; Graham, B. S.; McLellan, J. S.; Ward, A. B. Stabilized coronavirus spikes are resistant to conformational changes induced by receptor recognition or proteolysis. *Sci. Rep.* **2018**, *8*, No. 15701.
(9) Donoghue, M.; Hsieh, F.; Baronas, E.; Godbout, K.; Gosselin, M.; Stagliano, N.; Donovan, M.; Woolf, B.; Robison, K.; Jeyaseelan, R.; et al. A novel angiotensin-converting enzyme−related carboxypeptidase (ACE2) converts angiotensin I to angiotensin 1-9. *Circ. Res.* **2000**, *87*, e1−e9.
(10) Walls, A. C.; Park, Y.-J.; Tortorici, M. A.; Wall, A.; McGuire, A. T.; Veesler, D. Structure, function, and antigenicity of the SARS-CoV-2 spike glycoprotein. *Cell* **2020**, No. 1735.
(11) Chu, H.; Chan, C.-M.; Zhang, X.; Wang, Y.; Yuan, S.; Zhou, J.; Au-Yeung, R. K.-H.; Sze, K.-H.; Yang, D.; Shuai, H.; et al. Middle East respiratory syndrome coronavirus and bat coronavirus HKU9 both can utilize GRP78 for attachment onto host cells. *J. Biol. Chem.* **2018**, *293*, 11709−11726.
(12) Ibrahim, I. M.; Abdelmalek, D. H.; Elshahat, M. E.; Elfiky, A. A. COVID-19 spike-host cell receptor GRP78 binding site prediction. *J. Infect.* **2020**, *80*, 554−562.
(13) Sabirli, R.; Koseler, A.; Goren, T.; Turkcuer, I.; Kurt, O. High GRP78 levels in Covid-19 infection: A case-control study. *Life Sci.* **2021**, *265*, No. 118781.
(14) Allam, L.; Ghrifi, F.; Mohammed, H.; El Hafidi, N.; El Jaoudi, R.; El Harti, J.; Lmimouni, B.; Belyamani, L.; Ibrahimi, A. Targeting the GRP78-Dependant SARS-CoV-2 Cell Entry by Peptides and Small Molecules. *Bioinf. Biol. Insights* **2020**, *14*, No. 1177932220965505.
(15) Carlos, A. J.; Ha, D. P.; Yeh, D.-W.; Van Krieken, R.; Gill, P.; Machida, K.; Lee, A. GRP78 binds SARS-CoV-2 Spike protein and ACE2 and GRP78 depleting antibody blocks viral entry and infection in vitro. *bioRxiv* **2021**, No. 2021.01.20.427368.
(16) Elfiky, A. A.; Ibrahim, I. M. Host-cell recognition through GRP78 is enhanced in the new UK variant of SARS-CoV-2, in silico. *J. Infect.* **2021**, 186.
(17) Camini, F. C.; da Silva Caetano, C. C.; Almeida, L. T.; de Brito Magalhaes, C. L. Implications of oxidative stress on viral pathogenesis. *Arch. Virol.* **2017**, *162*, 907−917.
(18) Ntyonga-Pono, M.-P. COVID-19 infection and oxidative stress: an under-explored approach for prevention and treatment? *Pan Afr. Med. J.* **2020**, *35*, No. 12.
(19) Chang, R.; Mamun, A.; Dominic, A.; Le, N.-T. SARS-CoV-2 mediated endothelial dysfunction: the potential role of chronic oxidative stress. *Front. Physiol.* **2020**, *11*, No. 605908.
(20) Suhail, S.; Zajac, J.; Fossum, C.; Lowater, H.; McCracken, C.; Severson, N.; Laatsch, B.; Narkiewicz-Jodko, A.; Johnson, B.; Liebau, J.; et al. Role of Oxidative Stress on SARS-CoV (SARS) and SARS-CoV-2 (COVID-19) Infection: A Review. *Protein J.* **2020**, 644−656.
(21) Yusupov, M.; Privat-Maldonado, A.; Cordeiro, R. M.; Verswyvel, H.; Shaw, P.; Razzokov, J.; Smits, E.; Bogaerts, A. Oxidative damage to hyaluronan−CD44 interactions as an underlying mechanism of action of oxidative stress-inducing cancer therapy. *Redox Biol.* **2021**, *43*, No. 101968.
(22) Lin, A.; Razzokov, J.; Verswyvel, H.; Privat-Maldonado, A.; De Backer, J.; Yusupov, M.; Cardenas De La Hoz, E.; Ponsaerts, P.; Smits, E.; Bogaerts, A. Oxidation of Innate Immune Checkpoint CD47 on Cancer Cells with Non-Thermal Plasma. *Cancers* **2021**, *13*, No. 579.
(23) Yusupov, M.; Razzokov, J.; Cordeiro, R. M.; Bogaerts, A. Transport of Reactive Oxygen and Nitrogen Species across Aquaporin: A Molecular Level Picture. *Oxid. Med. Cell. Longevity* **2019**, *2019*, No. 2930504.
(24) Razzokov, J.; Yusupov, M.; Bogaerts, A. Oxidation destabilizes toxic amyloid beta peptide aggregation. *Sci. Rep.* **2019**, *9*, No. 5476.
(25) De Backer, J.; Razzokov, J.; Hammerschmid, D.; Mensch, C.; Hafideddine, Z.; Kumar, N.; van Raemdonck, G.; Yusupov, M.; Van Doorslaer, S.; Johannessen, C.; Sobott, F.; Bogaerts, A.; Dewilde, S. The effect of reactive oxygen and nitrogen species on the structure of cytoglobin: A potential tumor suppressor. *Redox Biol.* **2018**, *19*, 1−10.
(26) Yusupov, M.; Lackmann, J.-W.; Razzokov, J.; Kumar, S.; Stapelmann, K.; Bogaerts, A. Impact of plasma oxidation on structural features of human epidermal growth factor. *Plasma Processes Polym.* **2018**, *15*, No. 1800022.
(27) Katritzky, A. R.; Akhmedov, N. G.; Denisko, O. V. 1H and 13C NMR spectroscopic study of oxidation of d, l-cystine and 3, 3′-dithiobis (propionic acid) with hydrogen peroxide in aqueous solution. *Magn. Reson. Chem.* **2003**, *41*, 37−41.
(28) Takai, E.; Kitamura, T.; Kuwabara, J.; Ikawa, S.; Yoshizawa, S.; Shiraki, K.; Kawasaki, H.; Arakawa, R.; Kitano, K. Chemical modification of amino acids by atmospheric-pressure cold plasma in aqueous solution. *J. Phys. D: Appl. Phys.* **2014**, *47*, No. 285403.
(29) Xu, G.; Chance, M. R. Hydroxyl radical-mediated modification of proteins as probes for structural proteomics. *Chem. Rev.* **2007**, *107*, 3514−3543.
(30) Zhou, R.; Zhou, R.; Zhuang, J.; Zong, Z.; Zhang, X.; Liu, D.; Bazaka, K.; Ostrikov, K. Interaction of atmospheric-pressure air microplasmas with amino acids as fundamental processes in aqueous solution. *PLoS One* **2016**, *11*, No. e0155584.
(31) Bruno, G.; Heusler, T.; Lackmann, J.-W.; Von Woedtke, T.; Weltmann, K.-D.; Wende, K. Cold physical plasma-induced oxidation of cysteine yields reactive sulfur species (RSS). *Clin. Plasma Med.* **2019**, *14*, No. 100083.
(32) Hati, S.; Bhattacharyya, S. Impact of Thiol−Disulfide Balance on the Binding of Covid-19 Spike Protein with Angiotensin-Converting Enzyme 2 Receptor. *ACS Omega* **2020**, *5*, 16292−16298.
(33) Lan, J.; Ge, J.; Yu, J.; Shan, S.; Zhou, H.; Fan, S.; Zhang, Q.; Shi, X.; Wang, Q.; Zhang, L.; Wang, X. Structure of the SARS-CoV-2 spike receptor-binding domain bound to the ACE2 receptor. *Nature* **2020**, *581*, 215−220.
(34) Wiedemann, C.; Kumar, A.; Lang, A.; Ohlenschläger, O. Cysteines and disulfide bonds as structure-forming units: Insights from different domains of life and the potential for characterization by NMR. *Front. Chem.* **2020**, *8*, No. 280.
(35) Bechtel, T. J.; Weerapana, E. From structure to redox: The diverse functional roles of disulfides and implications in disease. *Proteomics* **2017**, *17*, No. 1600391.
(36) Cheng, T. M. K.; Blundell, T. L.; Fernandez-Recio, J. pyDock: Electrostatics and desolvation for effective scoring of rigid-body protein−protein docking. *Proteins: Struct., Funct., Bioinf.* **2007**, *68*, 503−515.
(37) Jiménez-García, B.; Pons, C.; Fernández-Recio, J. pyDockWEB: a web server for rigid-body protein−protein docking using electrostatics and desolvation scoring. *Bioinformatics* **2013**, *29*, 1698−1699.
(38) Kharasch, N. *Organic Sulfur Compounds*; Elsevier, 2013.
(39) Williams, B. J.; Barlow, C. K.; Kmiec, K. L.; Russell, W. K.; Russell, D. H. Negative ion fragmentation of cysteic acid containing peptides: cysteic acid as a fixed negative charge. *J. Am. Soc. Mass Spectrom.* **2011**, *22*, 1622−1630.
(40) Purdie, J. W. γ radiolysis of cystine in aqueous solution. Dose-rate effects and a proposed mechanism. *J. Am. Chem. Soc.* **1967**, *89*, 226−230.
(41) Wishart, D. S.; Feunang, Y. D.; Guo, A. C.; Lo, E. J.; Marcu, A.; Grant, J. R.; Sajed, T.; Johnson, D.; Li, C.; Sayeeda, Z.; Assempour, N.; Iynkkaran, I.; Liu, Y.; Maciejewski, A.; Gale, N.; Wilson, A.; Chin, L.; Cummings, R.; Le, D.; Pon, A.; Knox, C.; Wilson, M. DrugBank 5.0: a major update to the DrugBank database for 2018. *Nucleic Acids Res.* **2018**, *46*, D1074−D1082.
(42) Frisch, M.; Trucks, G.; Schlegel, H.; Scuseria, G.; Robb, M.; Cheeseman, J.; Scalmani, G.; Barone, V.; Petersson, G.; Nakatsuji, H.. *Gaussian 16*; Gaussian, Inc.: Wallingford, CT, 2016.
(43) Vanommeslaeghe, K.; Hatcher, E.; Acharya, C.; Kundu, S.; Zhong, S.; Shim, J.; Darian, E.; Guvench, O.; Lopes, P.; Vorobyov, I.; Mackerell, A. D., Jr. CHARMM general force field: A force field for drug-like molecules compatible with the CHARMM all-atom additive biological force fields. *J. Comput. Chem.* **2010**, *31*, 671−690.

https://doi.org/10.1021/acs.jcim.1c00853
J. Chem. Inf. Model. 2022, 62, 129−141

(44) van der Spoel, D.; van Maaren, P.; Caleman, C. GROMACS molecule & liquid database. *Bioinformatics* **2012**, *5*, 752−753.
(45) Abraham, M. J.; Murtola, T.; Schulz, R.; Páll, S.; Smith, J. C.; Hess, B.; Lindahl, E. GROMACS: High performance molecular simulations through multi-level parallelism from laptops to supercomputers. *SoftwareX* **2015**, *1*−*2*, 19−25.
(46) Bjelkmar, P.; Larsson, P.; Cuendet, M. A.; Hess, B.; Lindahl, E. Implementation of the CHARMM force field in GROMACS: analysis of protein stability effects from correction maps, virtual interaction sites, and water models. *J. Chem. Theory Comput.* **2010**, *6*, 459−466.
(47) Evans, D. J.; Holian, B. L. The nose−hoover thermostat. *J. Chem. Phys.* **1985**, *83*, 4069−4074.
(48) Parrinello, M.; Rahman, A. Polymorphic transitions in single crystals: A new molecular dynamics method. *J. Appl. Phys.* **1981**, *52*, 7182−7190.
(49) Darden, T.; York, D.; Pedersen, L. Particle mesh Ewald: An N· log (N) method for Ewald sums in large systems. *J. Chem. Phys.* **1993**, *98*, 10089−10092.
(50) Essmann, U.; Perera, L.; Berkowitz, M. L.; Darden, T.; Lee, H.; Pedersen, L. G. A smooth particle mesh Ewald method. *J. Chem. Phys.* **1995**, *103*, 8577−8593.
(51) Humphrey, W.; Dalke, A.; Schulten, K. VMD: visual molecular dynamics. *J. Mol. Graphics* **1996**, *14*, 33−38.
(52) Debiec, K. T.; Gronenborn, A. M.; Chong, L. T. Evaluating the strength of salt bridges: a comparison of current biomolecular force fields. *J. Phys. Chem. B* **2014**, *118*, 6561−6569.
(53) Biswal, H. S.; Shirhatti, P. R.; Wategaonkar, S. O− H··· O versus O− H··· S hydrogen bonding I: experimental and computational studies on the p-cresol· H2O and p-cresol· H2S complexes. *J. Phys. Chem. A* **2009**, *113*, 5633−5643.
(54) Gapsys, V.; Michielssens, S.; Seeliger, D.; de Groot, B. L. Accurate and rigorous prediction of the changes in protein free energies in a large-scale mutation scan. *Angew. Chem., Int. Ed.* **2016**, *55*, 7364−7368.
(55) Seeliger, D.; De Groot, B. L. Protein thermostability calculations using alchemical free energy simulations. *Biophys. J.* **2010**, *98*, 2309−2316.
(56) Aldeghi, M.; de Groot, B. L.; Gapsys, V. Accurate Calculation of Free Energy Changes upon Amino Acid Mutation. *Computational Methods in Protein Evolution*; Springer, 2019; pp 19−47.
(57) Yang, J.; Nune, M.; Zong, Y.; Zhou, L.; Liu, Q. Close and allosteric opening of the polypeptide-binding site in a human Hsp70 chaperone BiP. *Structure* **2015**, *23*, 2191−2203.
(58) Watanabe, K.; Watanabe, C.; Honma, T.; Tian, Y.-S.; Kawashima, Y.; Kawashita, N.; Takagi, T.; Fukuzawa, K. Intermolecular Interaction Analyses on SARS-CoV-2 Spike Protein Receptor Binding Domain and Human Angiotensin-Converting Enzyme 2 Receptor-Blocking Antibody/Peptide Using Fragment Molecular Orbital Calculation. *J. Phys. Chem. Lett.* **2021**, *12*, 4059−4066.
(59) Ngo, V. A.; Jha, R. K. Identifying key determinants and dynamics of SARS-CoV-2/ACE2 tight interaction. *PLoS One* **2021**, *16*, No. e0257905.
(60) Liu, H.; Lupala, C.; Li, X.; Lei, J.; Chen, H.; Qi, J.; Su, X. Computational simulations reveal the binding dynamics between human ACE2 and the receptor binding domain of SARS-CoV-2 spike protein. *bioRxiv* **2021**, No. 2021.11.30.470470.
(61) Hamann, M.; Zhang, T.; Hendrich, S.; Thomas, J. A. [15] Quantitation of protein sulfinic and sulfonic acid, irreversibly oxidized protein cysteine sites in cellular proteins. *Protein Sensors and Reactive Oxygen Species—Part B: Thiol Enzymes and Proteins*; Methods in Enzymology; Academic Press, 2002; Vol. *348*, pp 146−156.
(62) Attri, P.; Koga, K.; Shiratani, M. Possible impact of plasma oxidation on the structure of the C-terminal domain of SARS-CoV-2 spike protein: a computational study. *Appl. Phys. Express* **2021**, *14*, No. 027002.
(63) Guo, L.; Yao, Z.; Yang, L.; Zhang, H.; Qi, Y.; Gou, L.; Xi, W.; Liu, D.; Zhang, L.; Cheng, Y.; et al. Plasma-activated water: An alternative disinfectant for S protein inactivation to prevent SARS-CoV-2 infection. *Chem. Eng. J.* **2020**, No. 127742.
(64) Tu, Y.; Tang, W.; Yu, L.; Liu, Z.; Liu, Y.; Xia, H.; Zhang, H.; Chen, S.; Wu, J.; Cui, X.; et al. Inactivating SARS-CoV-2 by electrochemical oxidation. *Sci. Bull.* **2021**, *66*, 720−726.
(65) Carlos, A. J.; Ha, D. P.; Yeh, D.-W.; Van Krieken, R.; Tseng, C.-C.; Zhang, P.; Gill, P.; Machida, K.; Lee, A. S. The chaperone GRP78 is a host auxiliary factor for SARS-CoV-2 and GRP78 depleting antibody blocks viral entry and infection. *J. Biol. Chem.* **2021**, *296*, No. 100759.

https://doi.org/10.1021/acs.jcim.1c00853
J. Chem. Inf. Model. 2022, 62, 129−141